# Plasmon Modes and Hot Spots in Gold Nanostar-Satellite Clusters

Amane Shiohara[1], Sergey M. Novikov[1], Diego M. Solís[2], José M. Taboada[3], Fernando Obelleiro[2] and Luis M Liz-Marzán[1,4*]

[1]CIC biomaGUNE, Paseo de Miramón 182, 20009 Donostia-San Sebastián, Spain

[2]Departamento de Teoría de la Señal y Comunicaciones, University of Vigo, 36301 Vigo, Spain

[3]Departamento de Tecnología de los Computadores y de las Comunicaciones, University of Extremadura, 10003 Cáceres, Spain

[4]Ikerbasque, Basque Foundation for Science, 48011, Bilbao, Spain

* Corresponding author:

Prof. Luis M. Liz-Marzán

CIC biomaGUNE, Paseo de Miramón 182, 20009 Donostia-San Sebastián, Spain

Tel. +34 943005300

e-mail: llizmarzan@cicbiomagune.es

**Abstract**

Gold nanostars display strong electromagnetic field enhancement at their tips and tip plasmon resonances can be tuned within the visible and near infrared, which has been applied toward plasmonic molecular sensing. However, the sensitivity can be further increased by linking gold nanostars to other plasmonic nanoparticles and thereby inducing the creation of hot spots. We report the controlled formation of core-satellite assemblies comprising a central gold nanostar with gold spheres adsorbed to the tips *via* Raman active molecular linkers. Surface enhanced Raman scattering (SERS) was recorded at the level of single gold nanostar-satellite clusters and the experimental results were compared with detailed electromagnetic simulations.

**Keywords:** plasmonics, gold nanoparticles, modeling, SERS

## 1. Introduction

Surface Enhanced Raman scattering (SERS) is a powerful technique that provides structural information from minute amounts of molecular analytes, thus rendering it a promising technique for sensing applications. SERS relies on the unique optical properties of plasmonic metal nanoparticles,[1-4] since excitation of the corresponding localized surface plasmon resonances (LSPRs) leads to great enhancement of the local electric near field around the surface of the nanoparticles. The spectral position of LSPRs can be tuned through a variety of parameters such as the size and shape of the nanoparticles, which allows for example to study biological organisms with 785 nm laser excitation, *i.e.* within the biological transparency window.[5-6] In this respect, anisotropic nanoparticles with sharp tips can provide significantly large near field enhancements, as compared to spherical nanoparticles,[7-10] and are thus excellent SERS substrates.[11-18] For this reason, fabrication of metallic nanoparticles with pointed features, such as (bi)pyramids, triangles or stars has seen significant progress in recent years. Another efficient means to produce large field enhancement is the coupling of plasmon modes between closely spaced nanoparticles, so that so-called hot spots are created at interparticle gaps.[19-20] Therefore, several factors need to be considered when producing SERS substrates, such as the spectral position of the LSPR maximum, the eventual electronic resonance of the Raman probe molecules, and coverage of the probe molecules on the plasmonic surface. To establish a reliable, highly enhancing SERS substrate, precise characterization of the plasmonic system is essential, including an estimate of the potential sensitivity. Several studies on the SERS performance of colloidal nanoparticle aggregates have been reported,[21-25] most of them based on Ag or Au spherical particles, whereas the literature involving assemblies of anisotropic nanoparticles is much more scarce.[26] One of the most promising anisotropic nanoparticle systems comprises Au

nanostars, which have been shown to display huge near field enhancement, due to the presence of multiple sharp spikes.[27] The total SERS enhancement factor of a single Au nanostar was reported by Feldman et al.[28] to be $10^7$ under their measurement conditions. However, the SERS enhancement factor could be further increased by creating a core-satellite system in which metal nanoparticles are attached to a central metallic core. SERS measurements of core-satellite systems have been reported by several groups,[29-33] both using spherical nanoparticles[29-30, 33] and mixtures of nanorods and spheres.[31-32] We propose that a core-satellite design comprising gold nanostar cores may offer a promising direction toward establishing ultra-high enhancing SERS substrates. In this study we assembled core-satellite clusters comprising a central ~65 nm gold nanostar surrounded by 12 nm spherical gold nanoparticles at different concentrations, which allowed us to study the enhancing efficiency of this system. Fundamental studies that relate structure to function in plasmonic systems are expected to clarify fabrication needs toward creating most efficient SERS substrates. We compared the SERS sensitivity of the gold nanostar core – gold sphere satellite system with isolated gold nanostars on glass substrates, showing its potential for applications in biosensing.

## 2. Experimental Section

*Chemicals.* Tetrachloroauric acid tetrahydrate ($HAuCl_4 \cdot 4H_2O$), silver nitrate ($AgNO_3$), ascorbic acid, sodium dodecylsulfate (SDS), 3-aminopropyltriethoxysilane (APTES), trisodium citrate, 4-aminothiophenol (ATP), and O-[2-(3-mercaptopropionylamino)ethyl]-O′-methylpolyethylene glycol (mPEG-SH; M.W. 5000) were purchased from Sigma-Aldrich and used without further purification. Milli-Q water was used throughout all experiments. The glassware was washed with aqua regia prior to use.

*Synthesis of gold nanospheres and nanostars.* Citrate stabilized gold nanoparticles were prepared by adding 15 mL of 1% citrate solution to 100 mL of boiling 1 mM $HAuCl_4$ solution under vigorous stirring.[34] Boiling was continued for 15 min and then the solution was cooled down to room temperature. The nanoparticle solution was then stored at 4 ºC. The same gold nanoparticles (*d*=12nm) were used as seeds for nanostar growth.

Larger citrate stabilized gold nanoparticles (30 nm) were prepared by seeded growth.[35] Briefly, 1 mL of 25 mM $HAuCl_4$ was added to 150 mL of boiling 2.2 mM citrate solution, under vigorous stirring. The reaction solution was cooled down to 90 ºC and then 1 mL of 60 mM sodium citrate and 1 mL of 25 mM $HAuCl_4$ were sequentially injected (time delay ~ 2min). The same process was repeated up to 14 generations of gold nanoparticles.

Nanostars were prepared by a reported seed-mediated method.[34] For sample S1 (plasmon peak 700 nm, tip aspect ratio 1.7), 1 mL of the seed solution was added to 100 mL of 0.25 mM $HAuCl_4$ solution containing 100 µL of 1 M HCl. Quickly, 100 µL of 0.01 M SDS, 200 µL of 0.01 M $AgNO_3$ and 500 µL of 0.1M ascorbic acid were added at room temperature. For sample S2 (plasmon peak 820 nm, tip aspect ratio 2.4), the same procedure was used but using 50 µL of 1 M HCl and 500 µL of 0.01M $AgNO_3$. The solution was stirred for 30 s as the color of the solution rapidly turned from light pink to green blue (S1) or grey (S2). The solutions were then centrifuged at 3800 rpm for 90 min at 4 ºC and redispersed in different amounts of ethanol. The nanostar solutions were stored in the dark at 4 ºC.

*Deposition of nanostars on glass.* Glass slides were washed with piranha solution, extensively rinsed and stored in Milli-Q water. Silanization with amino functional groups was carried out by vertically soaking the slides in 5% APTES solution in ethanol at 40 ºC for 4 h. The slides were then washed with ethanol for 15 min, sonicated and oven dried. The modified glass substrates

were vertically immersed in the purified nanostar solution in ethanol overnight. For AFM Raman measurements, the glass substrates were vertically immersed in the purified nanostar solution in ethanol for 1 min. The glass-supported nanostars were rinsed with ethanol 3-fold and stored in the dark at 4 ºC.

*Assembly of nanospheres on nanostars.* The glass substrates with adsorbed gold nanostars were immersed in a $10^{-5}$ M ATP solution in ethanol ($10^{-6}$ M for AFM Raman) at room temperature for 2 h. They were subsequently rinsed 3-fold with ethanol and 2-fold with Milli-Q water and then immersed in the citrate coated gold nanoparticle solution at different concentrations for 2 h. C1: $[Au^0]=8.8x10^{-6}$ M, C2: $[Au^0]=1.8x10^{-5}$ M, C3: $[Au^0]=5.9x10^{-5}$ M, C4: $[Au^0]=8.8x10^{-5}$ M, C5: $[Au^0]=1.8x10^{-4}$ M, C6: $[Au^0]=8.8x10^{-4}$ M. For AFM Raman only C5 was used. The substrates were finally rinsed 3-fold with Milli-Q water.

*Characterization.* Optical characterization was performed using an UV-vis spectrophotometer (Agilent 8453). Glass substrates were fixed on the wall of a quartz cuvette and immersed in water. SEM images were obtained in an ESEM Quanta250 FEG (FEI, The Netherlands). Raman scattering measurements were performed in a confocal scanning Raman microscope (micro-Renishaw InVia Reflex system equipped with Peltier-cooled charge-coupled device (CCD) detectors). The configuration involved a 1200 lines/mm diffraction grating, a 100× objective (N.A.=0.85) and excitation wavelengths of 633 nm, P~0.5 mW and 785 nm, P~0.18 mW, integration time 10 s, (for SERS spectra of glass substrates) and 633 nm, P~1,2 mW, 600 lines/mm diffraction grating, integration time 1 s (for SERS mapping). SERS images (7 $\mu$m × 7 $\mu$m) were recorded by mapping the spatial dependence of SERS intensity integrated at the main Raman peaks within the shift range 1505-1655 $cm^{-1}$, for each of the 30×30 points in the scan. These scan-parameters were selected as a compromise to obtain a significant signal from ATP

without bleaching. AFM mapping was performed with a Bruker NanoScope V - MultiMode system. Morphologies of nanoparticles and nanostars were characterized by transmission electron microscopy (TEM; JEOL 2010; 120 keV).

*Optical modeling.* Spectral and near field enhancement simulations were carried out using a numerical method based on the surface integral equation-method of moments (SIE-MoM) formulation ($M^3$ solver).[36-38] With this methodology, the metallic nanostructures are replaced by equivalent electric and magnetic currents placed over the particle boundary surfaces and interfaces. From Maxwell's equations in integral form and the boundary conditions for the total fields we derive a set of SIEs for the unknown equivalent currents. These SIEs are subsequently discretized by applying a Galerkin MoM procedure in terms of a set of basis and testing functions, leading to a dense $N \times N$ matrix system of linear equations (being $N$ the number of basis functions used to expand the unknown equivalent currents). For the realistic simulation of the large-scale plasmonic systems considered here, the multilevel fast multipole algorithm-fast Fourier transform (MLFMA-FFT)[39-41] was used to expedite the matrix vector products in the framework of an iterative resolution of the SIE-MoM matrix system. This yields a high algorithmic efficiency —computational cost of $O(N\log N)$ per iteration in both memory and time— along with high-scalability via parallelization using multicore computer clusters. The simulations were carried out on a workstation with four 8-core Intel Xeon E7-4820 18 MB L3 cache processors at 2 GHz. A high surface mesh density was considered using 824,845 basis functions (1,649,690 unknowns) for the parameterization of the whole ensemble of 250 randomly positioned nanostars with their respective NPs, with an average mesh size of about 3.8 nm, ranging from 1/105 wavelengths for the shortest simulated wavelength to 1/289 for the longest. This mesh size was further reduced to about 2 nm to ensure high accuracy in the near-

field calculation of SERS enhancement. Otherwise, a minimum distance of 150 nm between nanostars was considered to make sure that no plasmon hybridization occurs during calculation of the spectra. It should be noted that, as far as the particles are far enough from each other (>30 nm), the calculated spectrum does not change. A relative error norm of $10^{-5}$ was considered to halt the Krylov iterative solver. Considering the above, the computation times per wavelength ranged from 470 to 1292 seconds, while the memory use ranged from 28.9 to 52.1 GB. The following data were used for the theoretical simulations: core radius R=15 nm, tip length from 10 to 26 nm (aspect ratio 1.8 nm), number of the tips 10; gap between nanostar tips and spheres ~1.1 nm, sphere radius 6, 8, 15 nm. Amount of attached NPs and not attached NPs around of a satellite system: control -just single star, Case 1= 3 NPs on the end of tips, 1 between tips, 0 around satellite system; Case 2=5 NPs on the end of tips, 1 between tips, 1 around satellite system; Case 3=7 NPs on the end of tips, 2 between tips, 6 around satellite system and Case 4= 11 NPs on the end of tips, 4 between tips, 8 around satellite system. Case 5= 4 NPs on the end of tips, 1 between tips, 2 around satellite system (for the NPs with radius 15 nm).

**3. Results and Discussion**

To evaluate the relevance of hot spot formation, the core-satellite system comprising Au nanostars (S1 AuNS) and Au nanoparticles (12 nm and 30 nm) was prepared directly on a glass slide. The core size of S1 AuNS was 29.2±4.5 nm and the tip length 18.1±8.4 nm (with aspect ratio 1.8±0.7) and the average number of tips was 10±1. AuNS were attached to the glass substrate through the amine group of APTES and the surface of the nanostars was modified with ATP (AuNS/ATP). The glass substrates with adsorbed gold nanostars were soaked in the

corresponding solutions of gold nanoparticles to allow NP-NS attachment through the ATP amine group (AuNS/ATP/AuNP). The fabrication process is schematically shown in **Figure 1a**.

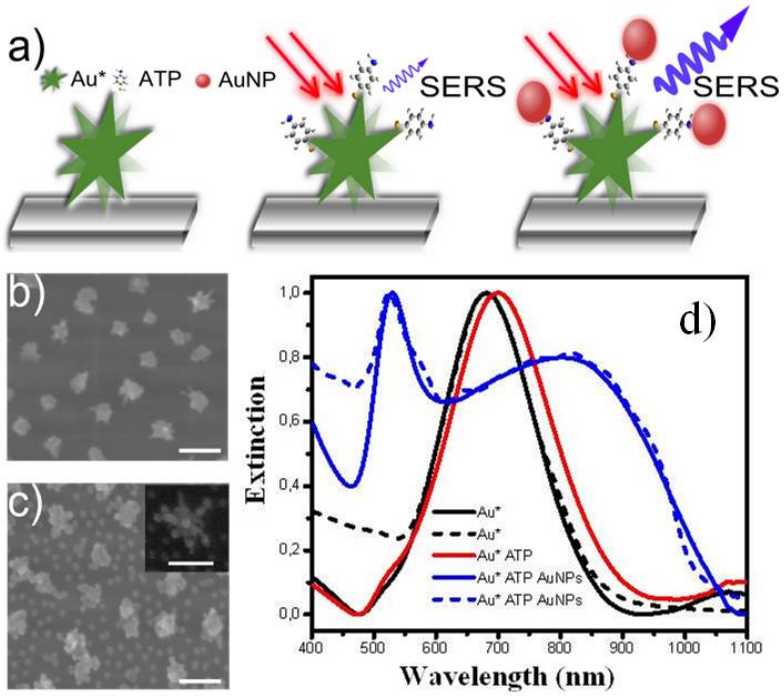


**Figure 1.** a) Schematic representation of the supported core-satellite preparation. AuNS were attached to a glass substrate through APTES and the AuNS surface was covered with ATP. AuNPs were adsorbed to the AuNS surface through the ATP amine groups, thereby creating SERS-active hot spots. b,c) SEM images of the AuNS on glass before (b) and after (c) adsorption of Au NPs. Inset: Zoom of the core-satellite particles. d) Experimental (solid lines) and simulated (dashed lines) extinction spectra of AuNS (black), AuNS/ATP (red), and AuNS/ATP/AuNP (blue). The scale bar is 100 nm in b and c, 75 nm in the inset.

The effect of the amount of AuNP per AuNS was studied by soaking the glass slides with AuNS in AuNP solutions at 6 different concentrations (C1-C6). SEM characterization clearly shows a

uniform distribution of both AuNS/ATP and AuNS/ATP/AuNP, as exemplified in Figure 1. Optical characterization was carried out by UV-vis spectroscopy upon immersing the particle-loaded glass substrates in water. Figure 1d shows the UV-vis spectra corresponding to the SEM images in Figure 1b,c (AuNS and AuNS/ATP/AuNP), while both SEM images and UV-Vis spectra for the complete study are shown in **Figure S1** (Supporting Information, SI). Whereas the plasmon peak of AuNS is centered at 680 nm, upon ATP adsorption it red-shifted by 15 nm, as expected from local refractive index variation. Upon attachment of AuNPs, the extinction at 400 nm significantly increased, indicating the presence of a larger amount of Au metal,[42] which also leads to an increased intensity at 520 nm, corresponding to the plasmon peak of well separated AuNPs. This can be explained upon examination of the SEM image in **Figure 1c**, which shows that AuNPs not only adsorb on AuNS/ATP, but also on the glass substrate, most likely via the APTES amine groups. Nevertheless, the broadening and red shift of the AuNS plasmon peak from 680 nm up to 750 nm, indicates adsorption of AuNP on AuNS, which can also be appreciated in the high resolution SEM image (inset of Figure 1c). The number of attached AuNP per AuNS was found to increase with AuNP concentration, such that for C1 and C2 almost no AuNP to AuNS adsorption was observed (**Figure S1**) while the number of AuNP per AuNS varied between 3-8 and 11-15 for C3- C6, respectively. This is also reflected in the UV-vis spectra as a broadening of the plasmon peak and an increase of the extinction at 400 nm. Optical simulations were carried out by using the so-called $M^3$ (M-cube, the newest version of the former HEMCUVE) surface integral-equation solver. This software combines an *ad hoc* implementation of the method of moments (MoM),[36-38] with the most recent advances in spectral acceleration techniques, based on the multilevel fast multipole algorithm (MLFMA) and the fast Fourier transform (FFT),[39-41] for the simulation of realistic large-scale plasmonic systems.

Calculated spectra for both AuNS and AuNS/ATP/AuNP satellite systems showed remarkably good agreement with the corresponding experimental data (**Figure 1d**). Around 250 randomly positioned stars were considered for the calculation of the AuNS spectrum, while the same amount of randomly positioned satellite systems corresponding to Case 4 were used to simulate the AuNS/ATP/AuNP spectrum (see Experimental Section for details). These spectra correspond to the control and C6 experimental samples respectively. Otherwise, taking into account that the tip lengths in real AuNS are 18±8 nm long, the simulation was made with a statistical distribution of the polydispersity adjusted to fit the experimental data (up to 21 different tip lengths between 10 and 26 nm). As a complementary characterization tool, atomic force microscopy (AFM) was used to determine the height of the core-satellite particles (**see Figure 2**). The measured size for NPs on the glass substrate was 12-14 nm as expected, while the height of the core-satellite system was ca. 65-80 nm, which corresponds to the total size considering one AuNS and one spherical nanoparticle protruding from its upper tip. The low density of AuNS on the AFM image, as compared to SEM images, results from special sample preparation for SERS measurements on single core-satellite assemblies.

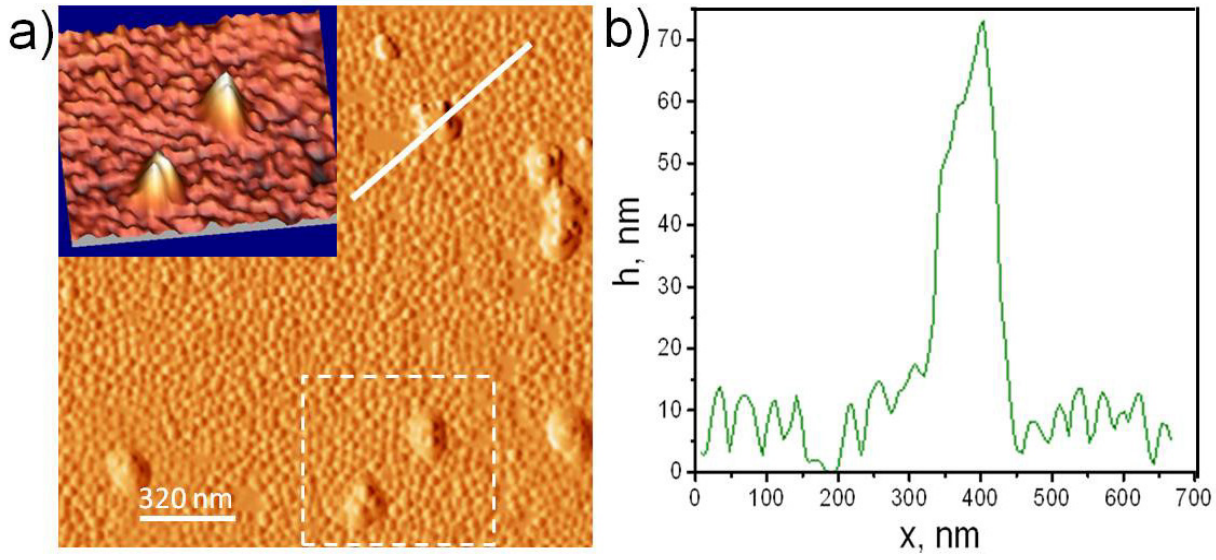

**Figure 2.** a) AFM topography image (1.4×1.4 $\mu m^2$) of the AuNS/ATP/AuNP core-satellites surrounded by AuNPs on the glass substrate. The inset shows a 3D rendering of the area marked by a white square (630×540 $nm^2$). b) Profile showing representative particle heights, as corresponding to line scans on a).

SERS characterization was performed on all AuNS/ATP/AuNP samples (C1-C6), as well as on AuNS/ATP, which was used as a control, with a 785 nm laser as the excitation source. The glass substrates were thoroughly washed with ethanol after immersion in ATP solution but prior to AuNP adsorption, so as to remove any free ATP and ensure that ATP SERS signals can originate only at either AuNS surfaces or at hot spots between AuNS and AuNP. In fact, no Raman scattering signals were recorded from a similar glass slide treated with ATP and AuNP, without AuNS. The probability to bind AuNP to AuNS was found to increase with increasing AuNP concentration, thereby creating a larger number of hot spots and leading to amplification of the Raman (SERS) signal, as shown in Figure 3a. For low AuNP concentration (C1, C2) the SERS intensities were similar to those of the control, AuNS/ATP (data not shown). We observed that the increasing number of hot spots did not affect equally all Raman peaks. The peak at 1590 $cm^{-1}$ (CC vibration) in Au NS gradually shifts when increasing Au NP concentration, up to 1570 $cm^{-1}$ (**Figure 3a, inset i**) at the maximum concentration of NPs (C6). This shift may result from conformational changes in the ring and contributions from a charge transfer (CT) mechanism for 4-ATP sandwiched between AuNS and AuNP,[43-45] caused by the increase in the number of NPs (*i.e.* increasing the number of AuNS/ATP/AuNP connections). Although with a slightly lower enhancement, a similar trend was observed in the SERS spectra recorded with an excitation wavelength of 633 nm (**Figure S2**). At the same time, for the strongest peak at 1082 $cm^{-1}$

assigned to CS stretching vibration, the intensity increased from AuNS/ATP to AuNS/ATP/AuNP with maximum concentration C6, but not dramatically as seen in the other peaks. No shifts were observed on the other peaks (**Figure 3a inset ii**). Furthermore, the ratio between the two main peaks $I_{1082}/I_{1590}$ was found to decrease for increasing amounts of AuNP, from 2.1 for AuNS/ATP down to 0.7 for AuNS/ATP/AuNP C6. The intensity of the peaks at 1143 $cm^{-1}$ (CH vibration) and at 1390 and 1432 $cm^{-1}$ (N=N) decreased by increasing the amount of AuNP and almost disappeared at maximum concentration (**Figure 3a**). These peaks are due to dimerization of ATP into 4,4'-dimercaptoazobenzene (DMAB) upon continuous laser excitation[46-47] whereas increased binding to AuNPs can prevent dimerization. Since field enhancement is localized at the hot spots, the SERS signal is dominated by molecules located in this area, where dimerization is quenched. The relative SERS enhancement was evaluated as the ratio between the intensity of the reference signal (AuNS/ATP) and AuNS/ATP/AuNP for the six readily identified Raman peaks, for different concentrations of AuNP (**Figure S3**). As shown in **Figure 3b**, the intensity of the Raman peak at 1590 $cm^{-1}$ gradually increased from C3 to C6, with a maximum enhancement of ca. 14 times for C6.

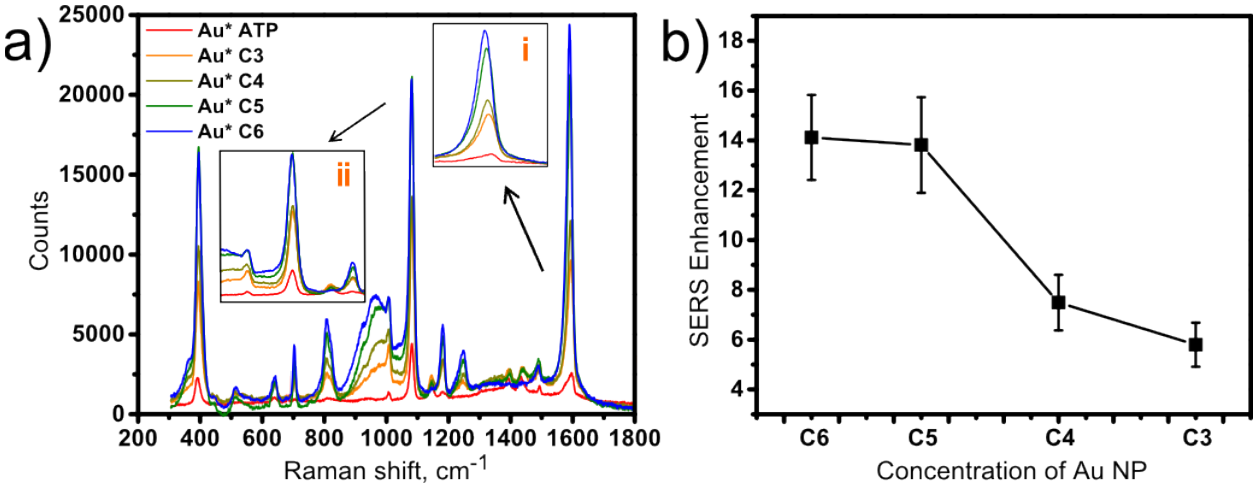

**Figure 3.** a) SERS spectra of ATP from AuNS/ATP, AuNS/ATP/AuNP at different concentrations of Au NPs (C3-6). Insets show enlarged views of the two main ATP peaks. b) Relative SERS enhancement factor as the ratio between the intensity of AuNS/ATP/AuNP with different AuNP concentrations (C3-C6) and the reference signal (AuNS/ATP), for the peak at 1590 $cm^{-1}$.

The LSPR modes of gold nanostar-satellites are strongly affected by the morphology of AuNS and the size of AuNP, in turn affecting the efficiency of SERS enhancement.[48] Therefore, we investigated the effect of varying the tip dimensions of AuNS with longer tips and higher aspect ratio (S2), which display a tip plasmon resonance at 820 nm. Again, the UV-vis spectra showed a gradual plasmon band broadening and increase of the absorbance at 400 nm, as the AuNP concentration was increased (**Figure S4**). In terms of SERS enhancement, the results are also equivalent, with a maximum 11-fold enhancement for C6. We also investigated the effect of AuNP size, by using 30 nm AuNP with both types of AuNS. Interestingly, when larger AuNPs were added, SEM images show the attachment of AuNP to AuNS only at the maximum particle concentration, which was also reflected in the extinction spectra (**Figure S5**). Maximum SERS enhancement (9.5 times larger than the control) was slightly lower than those obtained for smaller AuNPs, which is likely related to the smaller number of hot spots per Au NS.

A closer analysis of the efficiency of the hot spots between AuNS and AuNP was carried out by measuring SERS from single AuNS/ATP/AuNP core-satellite nanostructures. The specimen was prepared using AuNS S1 and 12 nm AuNP and the surface density of AuNS was controlled by immersing APTES modified glass substrates in the AuNS solution for 1 min. For SERS mapping of individual core-satellite particles a minimum distance around 3 μm between

nanostars was ensured. Figure 4a shows a representative SEM image of the nanostar-satellite system corresponding to the SERS mapping in Figure 4b, obtained by mapping integrated SERS intensity at the main Raman peaks within the shift range of 1505-1655 $cm^{-1}$, for each of the 30×30 pixels in the scan, with an integration time of 1 sec at each point (**Figure 4b inset**). A rough estimate (area of contact between the AuNS tip and spherical AuNP, and ATP footprint 0.2 $nm^2$) of the number of the molecules present in the hot spots of one core-satellite system yields a number of ~ 35 molecules per hot spot volume. Taking into account that each nanostar contains on average 10±1 tips and 2-3 of them are in contact with the glass substrate, the number of available ATP molecules would be around 240-300. This suggests that the main contribution of the SERS enhancement (**Fig 3b**) comes from this number of ATP molecules.

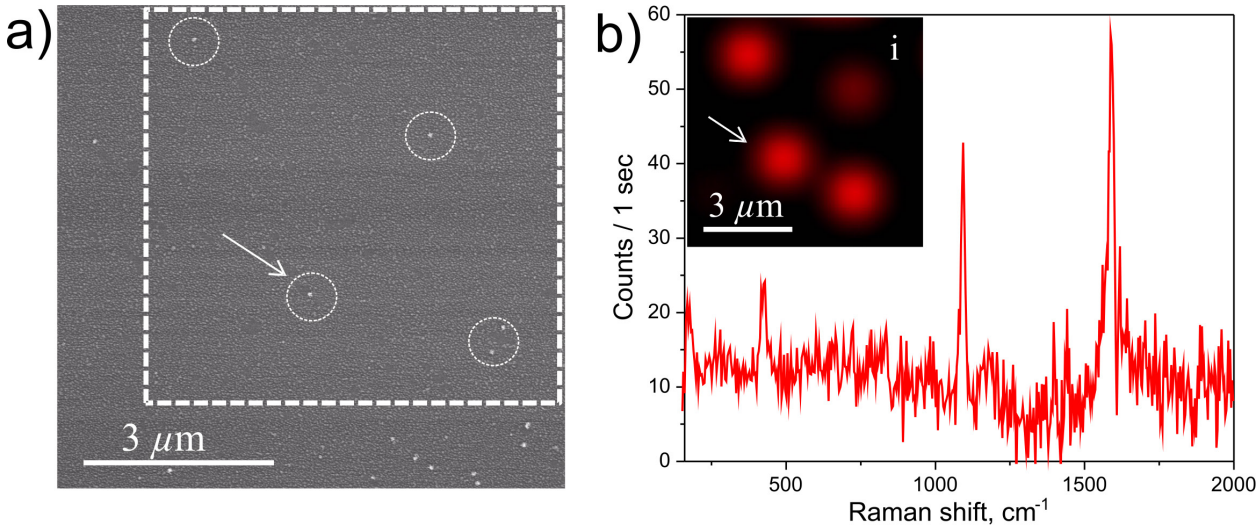


Figure 4. a) SEM image of individual core-satellite nanostructures. b) SERS spectrum obtained from the individual satellite indicated by a white arrow in a). The inset shows a SERS image (7 μm × 7 μm) obtained by mapping the SERS intensity integrated over the range 1505-1655 $cm^{-1}$ (the shaded column indicates the integration spectral range) from the dashed area on the SEM

image. The white circles around the particles in the SEM image, correspond to the spots in the SERS image.

Theoretical modeling was used to understand the obtained results. Simulations were carried out by means of the $M^3$ surface integral-equation solver, for a model based on a nanostar with conical spikes of equal tip length (18 nm) terminated by spheres located at 1.1 nm (the length of ATP) of the tip (**Figure 5**). Additional spheres were included to simulate the experimental systems with a larger amount of AuNP. Calculations were thus run for four AuNP concentrations (see Experimental Section for details), so that the number of attached and loose NPs was varied (**Figure 5a, insets**), including a control of nanostars alone, corresponding to the control and C3-C6 experimental samples. The dimensions of the particles for calculations were obtained from electron microscopy data.

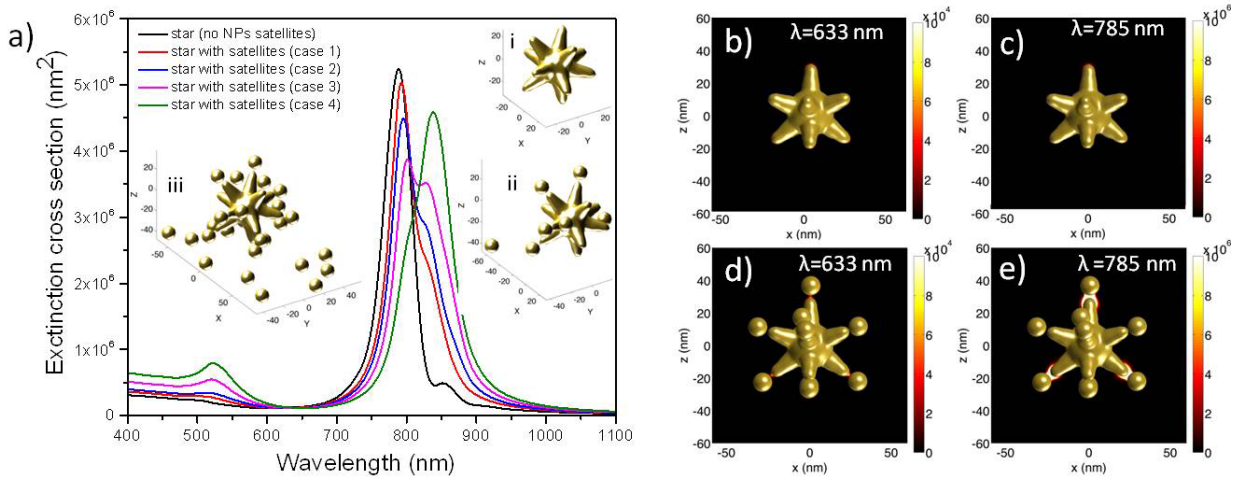


**Figure 5.** a) Calculated extinction cross-section spectra for a single nanostar and single core-satellite systems with increasing number of spheres, as shown in the insets for the pure nanostar (i), Case 2 (ii) and Case 4 (iii). Simulation of SERS enhancement (calculated as $|E|^4$ with electric

field amplitude E) for a vertically polarized incident plane wave coming from the right for a single nanostar (b.c) and the core-satellite system (d,e).

The results of the simulations indicate that the band around 520 nm gets enhanced with increasing number of satellite and non-attached (spectator) NPs. On the other hand, the band around 790 nm is slightly redshifted indicating plasmon coupling effects. A similar trend was observed for larger spheres, in agreement with the experimental results (**Figures S6, S7a**). Since the $M^3$ solver provides a large computational power,[36] around 250 randomly positioned nanostars (with their respective NPs) were considered in each simulation. The calculated spectra indicate that the AuNS tip mode is centered around 790 nm, while for the fully saturated core-satellite system (with spheres located near all the tips) the LSPR is at 840 nm. Intermediate cases correspond to random arrangements of nanostars with increasing number of satellite spheres, in which both types of resonances influence the overall spectra. Since the simulations of optical spectra agree well with the experimental spectra, SERS simulations were performed for the two excitation wavelengths of 633 and 785 nm (**Figure 5b-e**) that were used in the experiments. These simulations (calculated from the electric field amplitude E as $|E|^4$) were made for the incident plane wave from the right for a single nanostar and core-satellite system, with all tips linked to an AuNP). Figure 5b-e shows the results obtained for the nanostars with a tip length of 15 nm. From the simulation it is clear that significantly higher SERS enhancement is obtained when AuNP are located next to the AuNS, as compared to the bare AuNS. It is also clear that in both cases the enhancement for 785 nm excitation is higher than for 633 nm excitation, which agrees with a better overlap with the LSPR of the gap mode, reaching extremely large values $>10^{10}$ for the core-satellite case. However, since in real nanostars the tip length has a certain

variation (18.11±8.4 nm), simulations were carried out for nanostars with different tip lengths (10, 15 and 18 nm), which are displayed in Figures S8 and S9 (SI). The results can be summarized as follows: excitation with a 785 nm laser invariably leads to a stronger signal than the 633 nm laser, and additionally provides contributions from core-satellite systems with a wider range of tip lengths (**Figure S9**). The result from this stimulation allows us to estimate more correctly the number of molecules that contribute to SERS. As we mention above the main contribution to SERS enhancement (**Fig 3b**) comes from 240-300 ATP molecules. This calculation actually leads to an overestimate of the number of molecules. The linearly polarized laser excites a strong resonance only between combinations of nanostar tip and sphere with a favorable orientation (**Fig 5 b-e**). If we take this into account, the number of molecules giving the main contribution to the SERS signal would be around 120-150. Additionally, no significant differences were observed in the enhancement for satellite systems with AuNPs of radii of 6 and 15 nm. All these calculations correlate well and allow us to explain the obtained experimental results.

## 4. Conclusions

Aninothiophenol has been used to anchor gold nanoparticles to the tips of gold nanostars, creating a strongly coupled plasmonic gold nanostar-satellite system, both in solution and on glass surfaces. The formation of hot spots at the gaps was demonstrated by SERS spectroscopy of ATP, showing that the magnitude of near field and Raman scattering enhancement is directly related to the amount of AuNPs per AuNS. We found that the SERS signal of the core-satellite system can be up to ~14-fold higher than that for nanostars alone, with a maximum number of AuNPs per AuNS of 11±3. Interestingly, our results indicate that hot spot formation is almost

independent of AuNS tip morphology and AuNP size. The experimental results were confirmed by theoretical simulations based on a model that accurately reproduces the geometrical features of the real nanostructures. We propose that this nanostar-satellite system has a great potential not only as a model system to better understand hot spot formation, but also for applications such as sensing.

**Supporting Information available.** SEM images of AuNS-ATP-AuNP (C1-C6); SERS spectra of samples C3-C6 on glass substrate; SERS enhancement factors; extinction and SERS spectra of AuNS(S2)-ATP-AuNP and AuNS-ATP-AuNP(30 nm); additional calculated and SERS spectra. This material is available free of charge *via* the Internet at http://pubs.acs.org.

**Acknowledgements.** L.M.L.-M. acknowledges funding from the European Research Council (ERC Advanced Grant #267867 PLASMAQUO) and the Spanish Ministerio de Economía y Competitividad (MAT2013-46101-R). D.M.S., J.M.T., and F.O. acknowledge funding from the European Regional Development Fund (ERDF) and the Spanish Government, Ministerio de Economía y Competitividad (TEC2011-28784-C02-01, TEC2011-28784-C02-02, CONSOLIDER INGENIO 2010 CSD2008-00068, project TACTICA), from the ERDF and the Galician Regional Government under agreement for funding the atlantic Research Center for Information and Communication Technologies (atlantTIC), and from the ERDF and the Extremadura Regional Government (IB13185).

**References**

1. Grzelczak, M.; Perez-Juste, J.; Mulvaney, P.; Liz-Marzan, L. M. Shape Control in Gold Nanoparticle Synthesis. *Chem. Soc. Rev.* **2008**, *37*, 1783-1791.

2. Maier, S. A.; Brongersma, M. L.; Kik, P. G.; Meltzer, S.; Requicha, A. A. G.; Atwater, H. A. Plasmonics—a Route to Nanoscale Optical Devices. *Adv. Mater.* **2001**, *13*, 1501-1505.
3. Alvarez-Puebla, R.; Liz-Marzán, L. M.; García de Abajo, F. J. Light Concentration at the Nanometer Scale. *J. Phys. Chem. Lett.* **2010**, *1*, 2428-2434.
4. Kelly, K. L.; Coronado, E.; Zhao, L. L.; Schatz, G. C. The Optical Properties of Metal Nanoparticles: The Influence of Size, Shape, and Dielectric Environment. *J.Phys. Chem. B.* **2002**, *107*, 668-677.
5. Movasaghi, Z.; Rehman, S.; Rehman, I. U. Raman Spectroscopy of Biological Tissues. *Appl. Spectrosc. Rev.* **2007**, *42*, 493-541.
6. Notingher, I.; Verrier, S.; Romanska, H.; Bishop, A. E.; Polak, J. M.; Hench, L. L. In Situ Characterisation of Living Cells by Raman Spectroscopy. *Spectroscopy* **2002**, *16*, 43-51.
7. Kumar, P. S.; Pastoriza-Santos, I.; Rodríguez-González, B.; García de Abajo, F. J.; Liz-Marzán, L. M. High-Yield Synthesis and Optical Response of Gold Nanostars. *Nanotechnology* **2008**, *19*, 015606.
8. Hao, E.; Bailey, R. C.; Schatz, G. C.; Hupp, J. T.; Li, S. Synthesis and Optical Properties of "Branched" Gold Nanocrystals. *Nano Lett.* **2004**, *4*, 327-330.
9. Shao, L.; Susha, A. S.; Cheung, L. S.; Sau, T. K.; Rogach, A. L.; Wang, J. Plasmonic Properties of Single Multispiked Gold Nanostars: Correlating Modeling with Experiments. *Langmuir* **2012**, *28*, 8979-8984.
10. Hao, F.; Nehl, C. L.; Hafner, J. H.; Nordlander, P. Plasmon Resonances of a Gold Nanostar. *Nano Lett.* **2007**, *7*, 729-732.
11. Jana, N. R.; Pal, T. Anisotropic Metal Nanoparticles for Use as Surface-Enhanced Raman Substrates. *Adv. Mater.* **2007**, *19*, 1761-1765.
12. Chen, T.; Wang, H.; Chen, G.; Wang, Y.; Feng, Y.; Teo, W. S.; Wu, T.; Chen, H. Hotspot-Induced Transformation of Surface-Enhanced Raman Scattering Fingerprints. *ACS Nano* **2010**, *4*, 3087-3094.
13. Rodríguez-Lorenzo, L.; Álvarez-Puebla, R. A.; Pastoriza-Santos, I.; Mazzucco, S.; Stéphan, O.; Kociak, M.; Liz-Marzán, L. M.; García de Abajo, F. J. Zeptomol Detection through Controlled Ultrasensitive Surface-Enhanced Raman Scattering. *J. Am. Chem. Soc.* **2009**, *131*, 4616-4618.
14. Rodríguez-Lorenzo, L.; Alvarez-Puebla, R. A.; García de Abajo, F. J.; Liz-Marzán, L. M. Surface Enhanced Raman Scattering Using Star-Shaped Gold Colloidal Nanoparticles. *J. Phys. Chem. C.* **2009**, *114*, 7336-7340.
15. Ma, W.; Sun, M.; Xu, L.; Wang, L.; Kuang, H.; Xu, C. A SERS Active Gold Nanostar Dimer for Mercury Ion Detection. *Chem. Commun.* **2013**, *49*, 4989-4991.
16. Su, Q.; Ma, X.; Dong, J.; Jiang, C.; Qian, W. A Reproducible SERS Substrate Based on Electrostatically Assisted Aptes-Functionalized Surface-Assembly of Gold Nanostars. *ACS Appl. Mater. Interfaces* **2011**, *3*, 1873-1879.
17. Garcia-Leis, A.; García-Ramos, J. V.; Sanchez-Cortes, S. Silver Nanostars with High SERS Performance. *J. Phys. Chem. C.* **2013**, 117, 7791-7795.
18. Shiohara, A.; Langer, J.; Polavarapu, l.; Liz-Marzan, L. M. Solution Processed Polydimethylsiloxane/ Gold Nanostar Flexible Substrates for Plasmonic Sensing. *Nanoscale* **2014**, *6*, 9817–9823.
19. Kleinman, S. L.; Sharma, B.; Blaber, M. G.; Henry, A.-I.; Valley, N.; Freeman, R. G.; Natan, M. J.; Schatz, G. C.; Van Duyne, R. P. Structure Enhancement Factor Relationships in

Single Gold Nanoantennas by Surface-Enhanced Raman Excitation Spectroscopy. *J. Am. Chem. Soc.* **2012**, *135*, 301-308.
20. Camden, J. P.; Dieringer, J. A.; Wang, Y.; Masiello, D. J.; Marks, L. D.; Schatz, G. C.; Van Duyne, R. P. Probing the Structure of Single-Molecule Surface-Enhanced Raman Scattering Hot Spots. *J. Am. Chem. Soc.* **2008**, *130*, 12616-12617.
21. Hu, J.; Zheng, P.-C.; Jiang, J.-H.; Shen, G.-L.; Yu, R.-Q.; Liu, G.-K. Sub-Attomolar HIV-1 DNA Detection Using Surface-Enhanced Raman Spectroscopy. *Analyst* **2010**, *135*, 1084-1089.
22. Zhang, Z.; Wen, Y.; Ma, Y.; Luo, J.; Zhang, X.; Jiang, L.; Song, Y. Enhanced Nanoparticle-Oligonucleotide Conjugates for DNA Nanomachine Controlled Surface-Enhanced Raman Scattering Switch. *Appl. Phys. Lett.* **2011**, *98*, 133774.
23. Taladriz-Blanco, P.; Buurma, N. J.; Rodriguez-Lorenzo, L.; Perez-Juste, J.; Liz-Marzan, L. M.; Herves, P. Reversible Assembly of Metal Nanoparticles Induced by Penicillamine. Dynamic Formation of Sers Hot Spots. *J. Mater. Chem.* **2011**, *21*, 16880-16887.
24. Fabris, L.; Dante, M.; Nguyen, T.-Q.; Tok, J. B. H.; Bazan, G. C. SERS Aptatags: New Responsive Metallic Nanostructures for Heterogeneous Protein Detection by Surface Enhanced Raman Spectroscopy. *Adv. Funct. Mater.* **2008**, *18*, 2518-2525.
25. Saha, A.; Palmal, S.; Jana, N. R. Highly Reproducible and Sensitive Surface-Enhanced Raman Scattering from Colloidal Plasmonic Nanoparticle Via Stabilization of Hot Spots in Graphene Oxide Liquid Crystal. *Nanoscale* **2012**, *4*, 6649-6657.
26. Potara, M.; Gabudean, A.-M.; Astilean, S. Solution-Phase, Dual LSPR-SERS Plasmonic Sensors of High Sensitivity and Stability Based on Chitosan-Coated Anisotropic Silver Nanoparticles. *J. Mater. Chem.* **2011**, *21*, 3625-3633.
27. Guerrero-Martínez, A.; Barbosa, S.; Pastoriza-Santos, I.; Liz-Marzán, L. M. Nanostars Shine Bright for You: Colloidal Synthesis, Properties and Applications of Branched Metallic Nanoparticles. *Curr. Op. Colloid Interface Sci.* **2011**, *16*, 118-127.
28. Hrelescu, C.; Sau, T. K.; Rogach, A. L.; Jäckel, F.; Feldmann, J. Single Gold Nanostars Enhance Raman Scattering. *Appl. Phys. Lett.* **2009**, *94*, 153113.
29. Kim, N. H.; Lee, S. J.; Moskovits, M. Reversible Tuning of Sers Hot Spots with Aptamers. *Adv. Mater.* **2011**, *23*, 4152-4156.
30. Chen, S.-Y.; Lazarides, A. A. Quantitative Amplification of Cy5 Sers in 'Warm Spots' Created by Plasmonic Coupling in Nanoparticle Assemblies of Controlled Structure. *J. Phys. Chem. C.* **2009**, *113*, 12167-12175.
31. Wang, Y.; Lee, K.; Irudayaraj, J. SERS Aptasensor from Nanorod-Nanoparticle Junction for Protein Detection. *Chem. Commun.* **2010**, *46*, 613-615.
32. Xu, L.; Kuang, H.; Xu, C.; Ma, W.; Wang, L.; Kotov, N. A. Regiospecific Plasmonic Assemblies for in Situ Raman Spectroscopy in Live Cells. *J. Am. Chem. Soc.* **2011**, *134*, 1699-1709.
33. Gandra, N.; Abbas, A.; Tian, L.; Singamaneni, S. Plasmonic Planet–Satellite Analogues: Hierarchical Self-Assembly of Gold Nanostructures. *Nano Lett.* **2012**, *12*, 2645-2651.
34. Yuan, H.; Khoury, C. G.; Hwang, H.; Wilson, C. M.; Grant, G. A.; Vo-Dinh, T. Gold Nanostars: Surfactant-Free Synthesis, 3D Modelling, and Two-Photon Photoluminescence Imaging. *Nanotechnology* **2012**, *23*, 075102.
35. Bastús, N. G.; Comenge, J.; Puntes, V. Kinetically Controlled Seeded Growth Synthesis of Citrate-Stabilized Gold Nanoparticles of up to 200 Nm: Size Focusing Versus Ostwald Ripening. *Langmuir* **2011**, *27*, 11098-11105.

36. Taboada, J. M.; Rivero, J.; Obelleiro, F.; Araújo, M. G.; Landesa, L. Method-of-Moments Formulation for the Analysis of Plasmonic Nano-Optical Antennas. *J. Opt. Soc. Am. A* **2011**, *28*, 1341-1348.
37. Harrington, R. F.; Harrington, J. L. *Field Computation by Moment Methods*; Oxford University Press. 1996, p 240.
38. Solís, D. M.; Taboada, J. M.; Obelleiro, F.; Liz-Marzán, L. M.; García de Abajo, F. J. Toward Ultimate Nanoplasmonics Modeling. *ACS Nano* **2014**, *8*, 7559-7570.
39. Taboada, J. M.; Araujo, M. G.; Basteiro, F. O.; Rodriguez, J. L.; Landesa, L. MLFMA-FFT Parallel Algorithm for the Solution of Extremely Large Problems in Electromagnetics. *Procs. IEEE* **2013**, *101*, 350-363.
40. Araújo, M. G.; Taboada, J. M.; Rivero, J.; Solís, D. M.; Obelleiro, F. Solution of Large-Scale Plasmonic Problems with the Multilevel Fast Multipole Algorithm. *Opt. Lett.* **2012**, *37*, 416-418.
41. Jiming, S.; Cai-Cheng, L.; Weng Cho, C. Multilevel Fast Multipole Algorithm for Electromagnetic Scattering by Large Complex Objects. *IEEE Trans. Ant. Propag.* **1997**, *45*, 1488-1493.
42. Scarabelli, L.; Grzelczak, M.; Liz-Marzán, L. M. Tuning Gold Nanorod Synthesis through Prereduction with Salicylic Acid. *Chem. Mater.* **2013**, *25*, 4232-4238.
43. Hu, X.; Wang, T.; Wang, L.; Dong, S. Surface-Enhanced Raman Scattering of 4-Aminothiophenol Self-Assembled Monolayers in Sandwich Structure with Nanoparticle Shape Dependence: Off-Surface Plasmon Resonance Condition. *J. Phys. Chem. C* **2007**, *111*, 6962-6969.
44. Zhou, Q.; Li, X.; Fan, Q.; Zhang, X.; Zheng, J. Charge Transfer between Metal Nanoparticles Interconnected with a Functionalized Molecule Probed by Surface-Enhanced Raman Spectroscopy. *Angew. Chem. Int. Ed.* **2006**, *45*, 3970-3973.
45. Torma, V.; Vidoni, O.; Simon, U.; Schmid, G. Charge-Transfer Mechanisms between Gold Clusters. *Eur. J. Inorg. Chem.* **2003**, *2003*, 1121-1127.
46. Huang, Y.-F.; Zhu, H.-P.; Liu, G.-K.; Wu, D.-Y.; Ren, B.; Tian, Z.-Q. When the Signal Is Not from the Original Molecule to Be Detected: Chemical Transformation of Para-Aminothiophenol on Ag During the Sers Measurement. *J. Am. Chem. Soc.* **2010**, *132*, 9244-9246.
47. Xu, P.; Kang, L.; Mack, N. H.; Schanze, K. S.; Han, X.; Wang, H.-L. Mechanistic Understanding of Surface Plasmon Assisted Catalysis on a Single Particle: Cyclic Redox of 4-Aminothiophenol. *Sci. Rep.* **2013**, *3*, 2997
48. Rodriguez-Lorenzo, L.; Krpetic, Z.; Barbosa, S.; Alvarez-Puebla, R. A.; Liz-Marzan, L. M.; Prior, I. A.; Brust, M. Intracellular Mapping with Sers-Encoded Gold Nanostars. *Integr. Biol.* **2011**, *3*, 922-926.

**Table of Contents Graphic**